Geologie en Mijnbouw **77:** 189–201, 1999.

Applications of remote sensing in geology

Appendix

Colour figures

The colour figures reproduced in black and white in the preceding pages of this Special Issue are presented in colour in this Appendix. They belong to the articles by Reeves, Zhang et al., Seijmonsbergen, Van der Meer, Tromp & Epema, and Klees & Massonnet.

Colin V. Reeves
Geological remote sensing in aerospace and time. Introduction

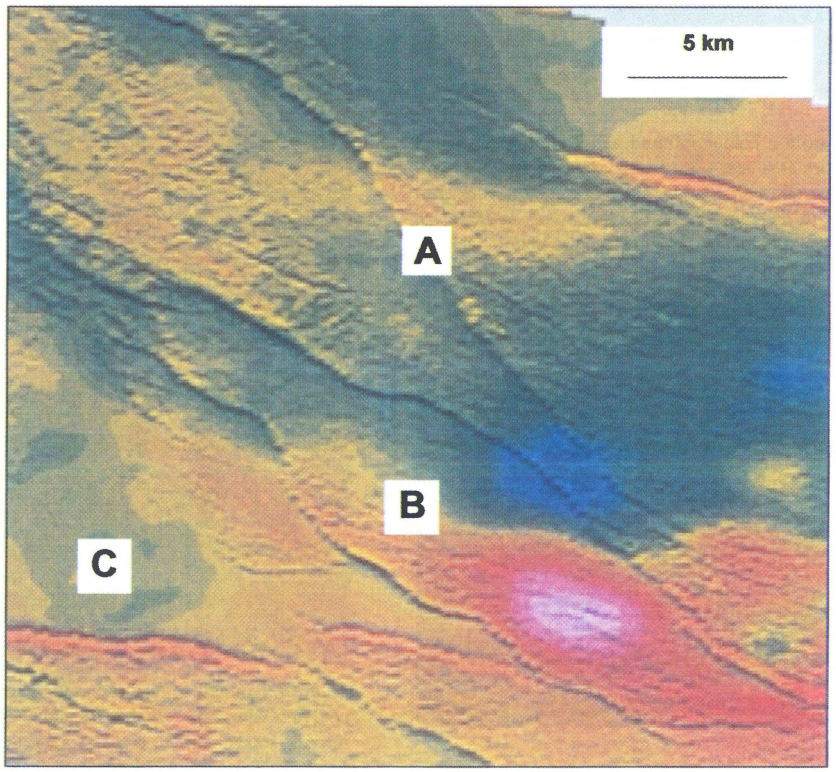

Figure 3. High-resolution, low-altitude aeromagnetic survey coverage of part of the Palla Road survey area in eastern Botswana. Interpretation of faults and fractures (such as A) cutting a thick (several hundred metres) basalt sheet underlying Kalahari sand cover – in conjunction with satellite imagery – is invaluable to ground-water exploration. A porous sandstone, stratigraphically below the basalt, is a productive aquifer where overlain by basalt (revealed by the speckle it imparts to the magnetic image, e.g. at B) but much less so where the basalt is absent (such as at C); (Barritt et al. 1995).

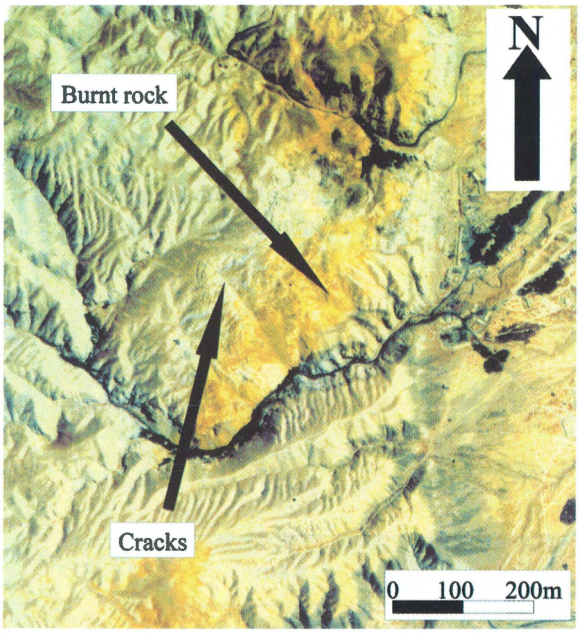

Figure 2. Extract from a colour infrared aerial photograph of an underground coal-fire area near Liuzhuangzi, taken 7 August 1992. Note the distinctive yellowish orange colour of the burnt rock. Immediately adjacent to the central area of burnt rock, an extensive area of land subsidence is indicated by the long, parallel cracks in the land surface.

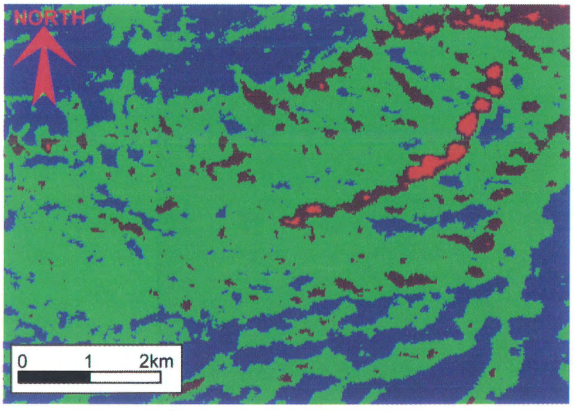

Figure 3. Night-time thermal infrared image acquired by the Landsat-TM over the Kelazha anticline coal-fire area in Xinjiang region on 7 April 1995. The image has been colour-coded and density-sliced. The areas in bright red indicate the location of underground coal fires.

Figure 4. Land subsidence occurring as a result of underground coal fires, Helanshan Mountains. The cracks are typically 20 cm to several metres wide, up to hundreds of metres long, and 10 to 20 m in depth. The process is illustrated in Figure 5.

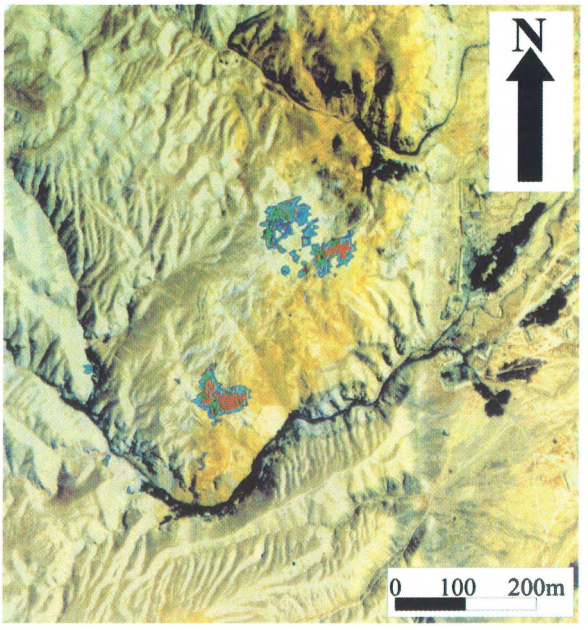

Figure 9. Example of feature-based image fusion for the detection of coal fires with respect to thermal anomalies derived from the thermal infrared image and the cracks shown in the colour infrared photograph. Paleo-coal-fire at Liuzhuangzi at top center (deep yellow; cf. Figure 2) is clearly distinguishable from present fires.

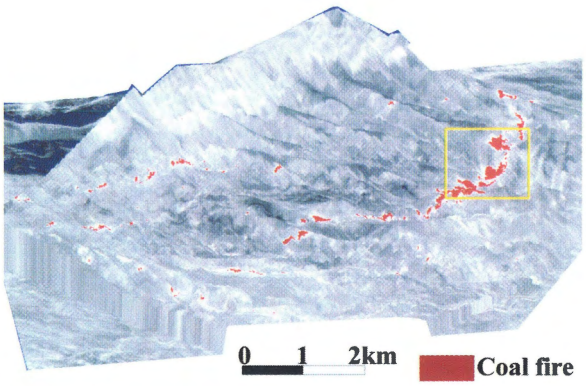

Figure 10. Airborne thermal infrared image data draped over and co-registered with the DEM to create a 3-D perspective view (due to the stretching at some places individual pixels can be seen) of Kelazha anticline coal-fire area (cf. Figure 3). Such products assist in the study of underground coal fires as they show the influence of topographic variables on the distribution of the fires. This view is looking in an ENE direction. Box outlines area of Figure 11.

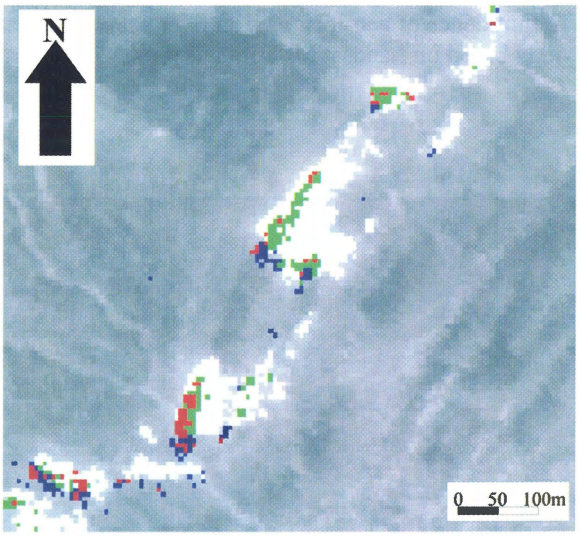

Figure 11. Example of decision-based image fusion for the detection of different intensive coal fires. The red areas represent the most intensive coal-fire areas derived from the 3–5 μm data. The green areas represent the middle-intensive coal fires derived from the day-time thermal infrared data of 8–12.5 μm. The white areas are the low-intensive coal fires derived from the night-time thermal infrared data of 8–12.5 μm data. The blue areas are the intensively solar-heated area. Individual pixels can be seen on the image. For location see Figure 10.

A.C. Seijmonsbergen

The influence of neo-tectonics on river patterns in Bangladesh; a preliminary study based on Landsat MSS imagery

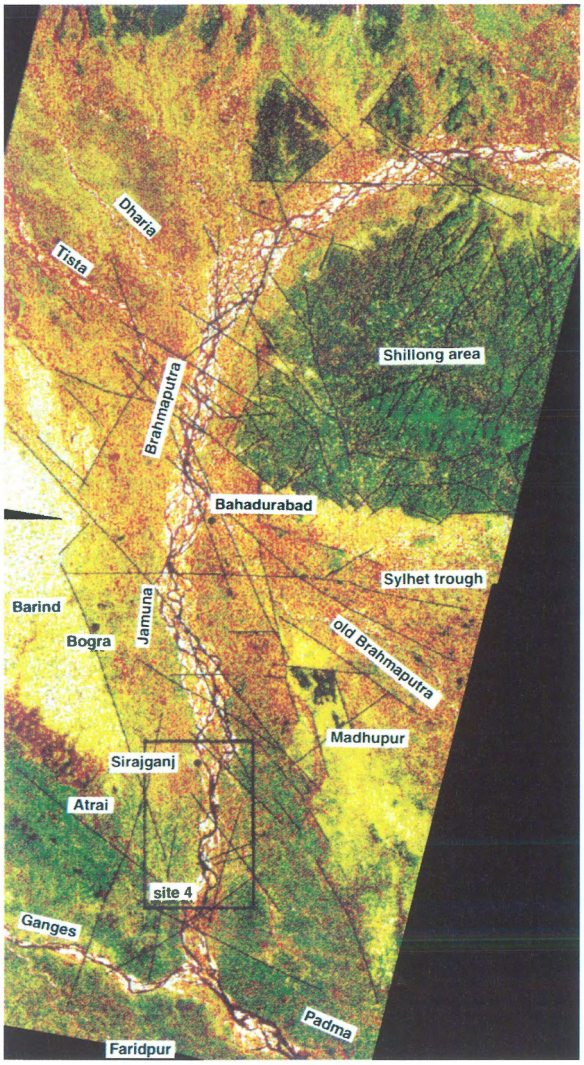

Figure 2. Classified 1978 Landsat MSS image of the area of interest, covering the course of the Jamuna. Interpreted lineaments are indicated. Window area indicates site 4, as shown in Figure 3. North to the top. Image size is ca. 320 km in N–S direction and between 160 and 100 km in E–W direction. Colours are explained in the text.

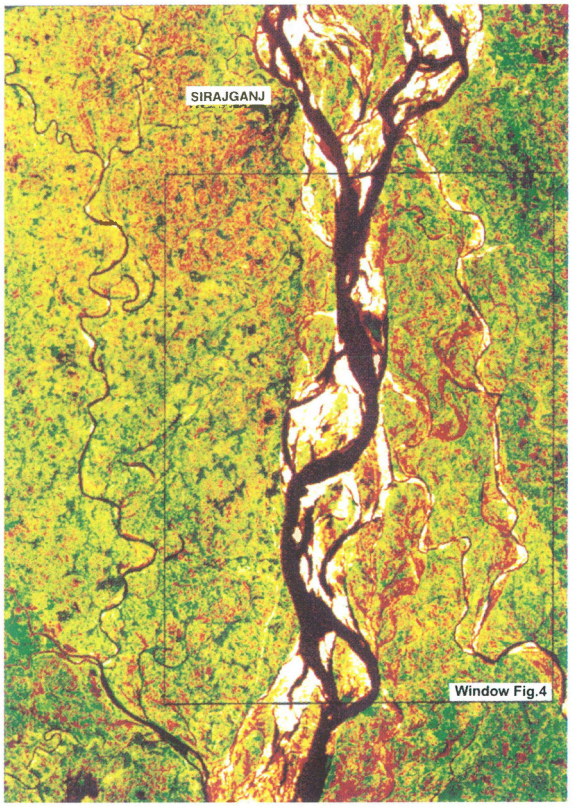

Figure 3. This fragment of the classified Landsat MSS image of 1978 has a colour scheme that approaches natural colours and proved to be most useful in the recognition of geological lineaments. The fragment covers test site no. 4 south of Sirajganj as indicated in Figure 2. Window area is seen in Figure 4. North to the top; image size is ca. 50 km in N–S and 34 km in E–W direction.

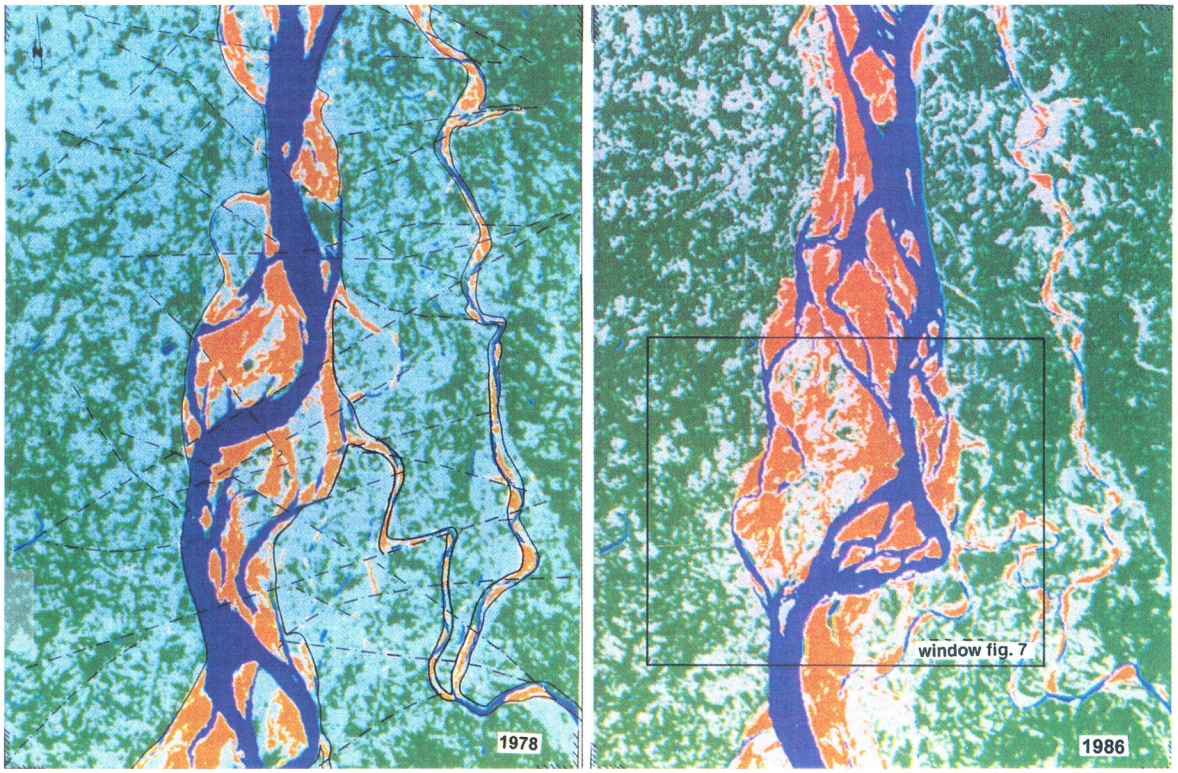

Figure 4. Comparison of 1978 (left) and 1986 (right) classified images showing lateral migration of Jamuna river course. Classification based on simple legend (blue = water, orange = sand bars, green and grey = dry land). Notice the lineament near a major bend in the river (cf. Figure 7). Interpreted lineaments indicative of faulting are shown on the 1978 classification. North to the top; image size is ca. 33 km in N–S, and 24 km in E–W direction. For location see Figure 3.

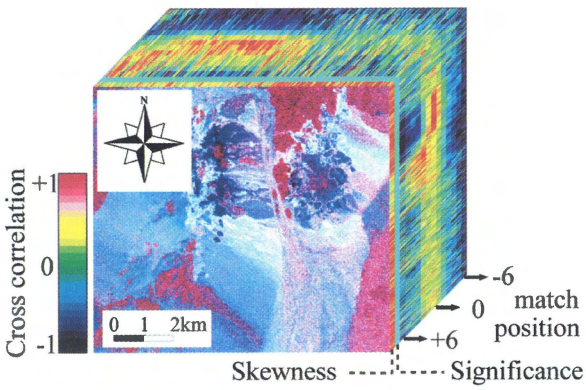

Figure 3. '3D' image correlogram cube for alunite. The face of the cube is a colour composite image of the area shown in Figure 2. (red = skewness; green = significance; blue = cross correlation at $M = 0$). Pixels similar to the mineral tested appear in white. The sides of the cube are spectral slices built up of cross correlogram images for the 13 match positions calculated. The correlation is coded using the colour scheme indicated by the bar (after Van der Meer & Bakker 1997b).

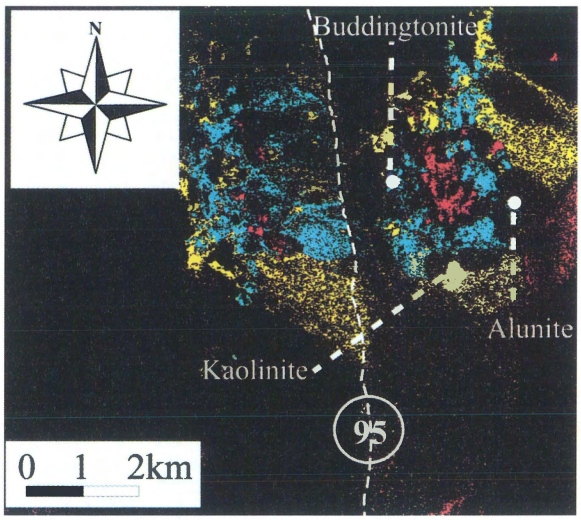

Figure 5. Final classification and alteration map for the Cuprite mining district, from AVIRIS data using the cross correlogram spectral matching technique. The scene is classified into kaolinite (yellow), alunite (cyan), silica (red) and buddingtonite (dark blue). Shown are pixels that have a cross correlation at $M = 0$, a skewness and a significance all exceeding 0.9 (after Van der Meer & Bakker 1998).

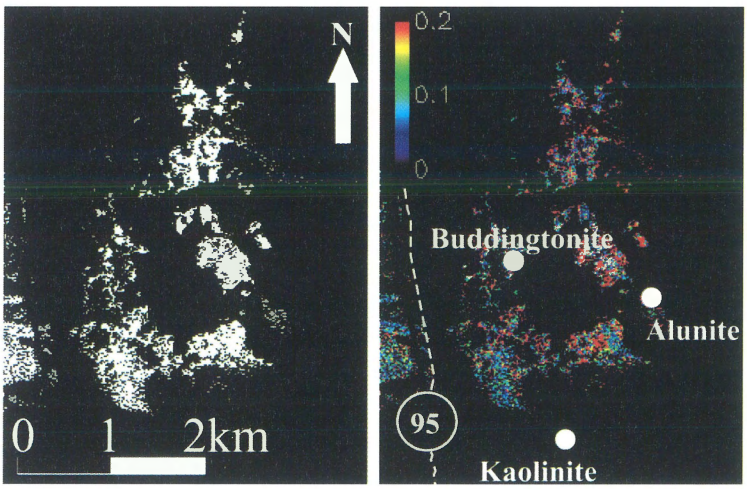

Figure 4. The image on the left shows the pixels classified as alunite in the northwestern part of the Cuprite mining district, using the cross correlogram spectral matching technique applied to AVIRIS data. The image on the right shows the root-mean-squared difference of the true and estimated pixel cross correlogram (after Van der Meer & Bakker 1998). See Figure 2 for location.

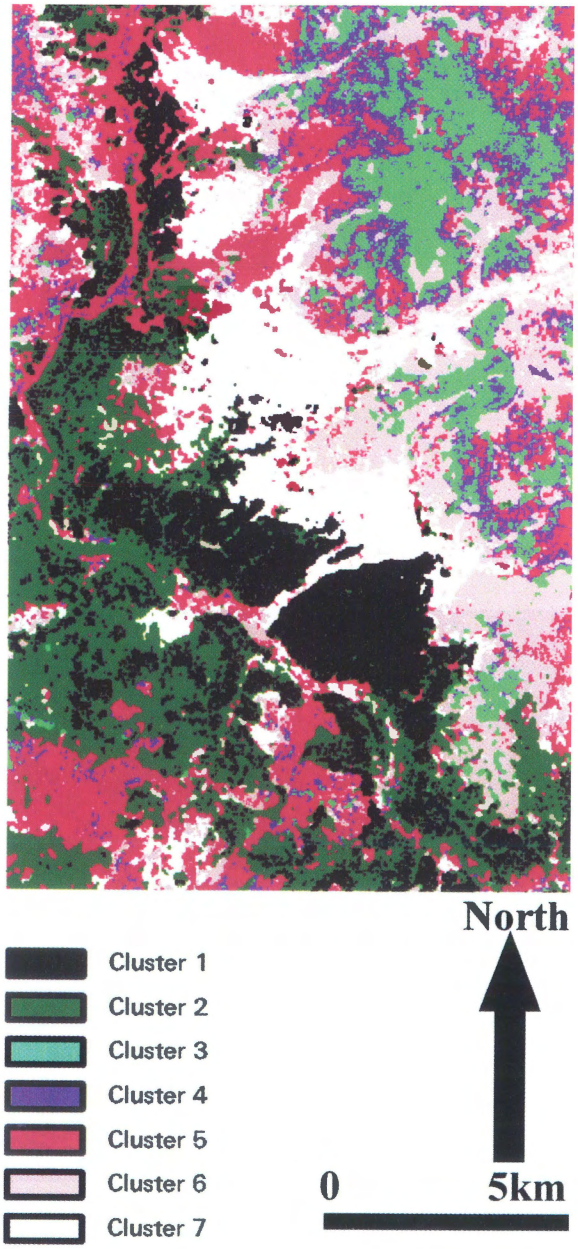

Figure 5. Unsupervised classification with the output images of the SMA using a Landsat TM data set acquired in May 1994 over the Sanmatenga site.

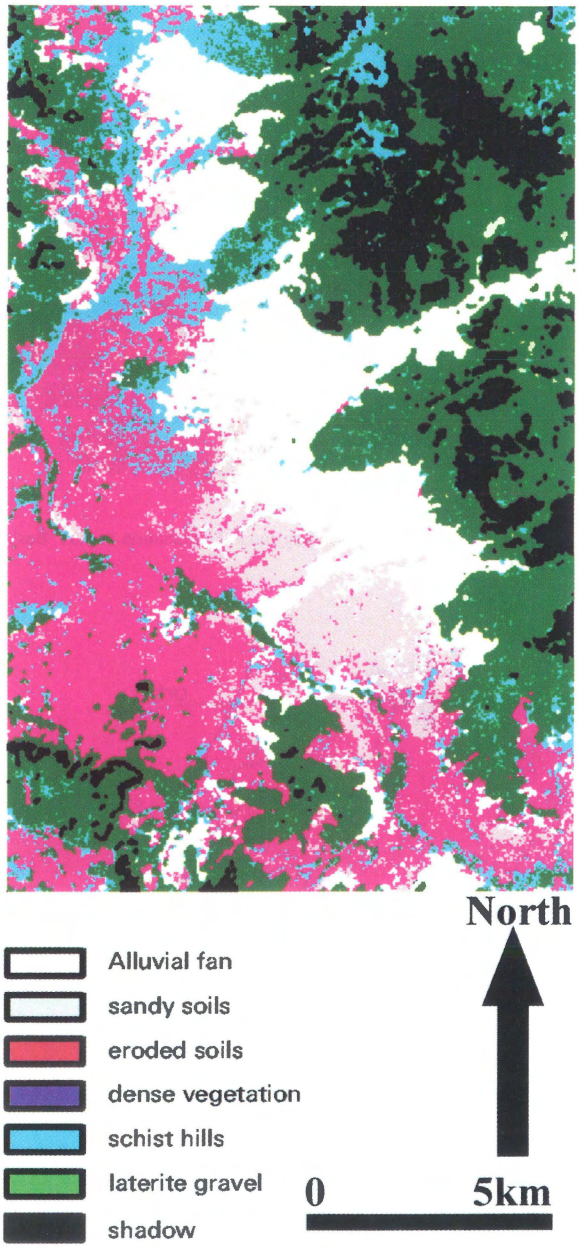

Figure 7. Maximum likelihood classification with the original spectral bands using a Landsat TM data set acquired in May 1994 over the Sanmatenga site.

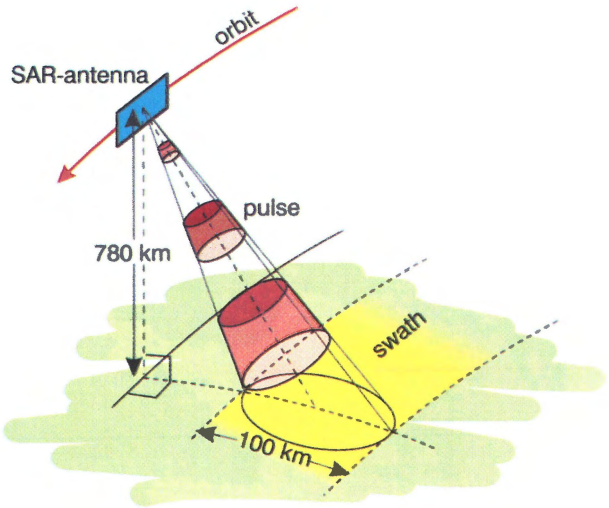

Figure 1. Geometry of an imaging radar. Explanation in text 'Basic principles'.

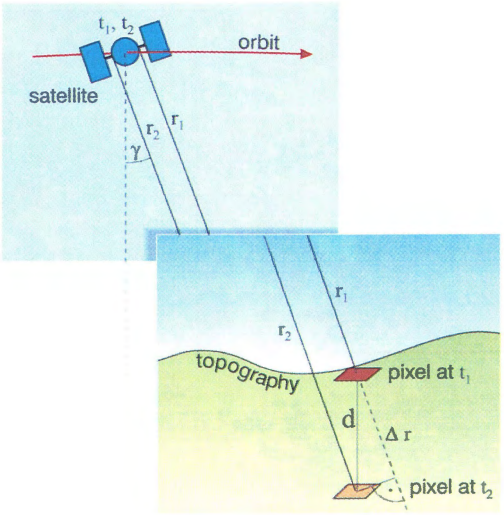

Figure 3. Geometry of InSAR with zero baseline.

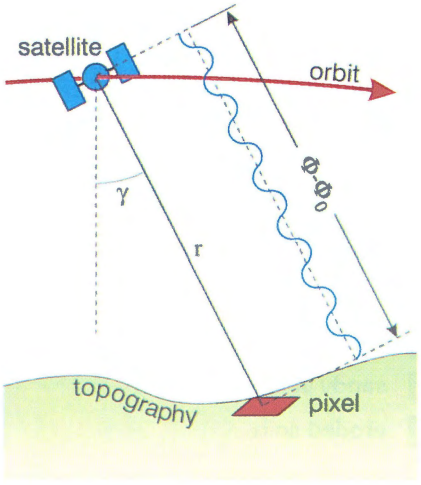

Figure 2. Slant range – phase relation.

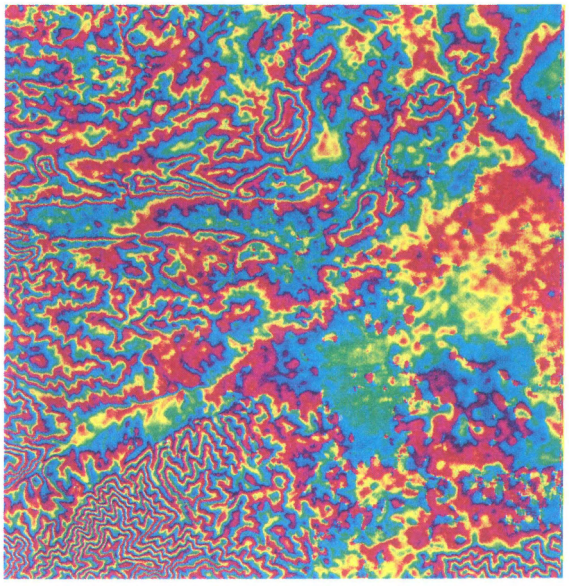

Figure 4. Fractional phase difference image (interferogram) from an area near Perpignan, France. The interferogram is dominated by the topographic fringes from the nearby Pyrenees mountain range. It also contains a contribution from a small earthquake that struck the area in January 1996, and various, small contributions from atmospheric delays. North to the top; scale is 100 m a pixel; area covered is ca. 50 × 50 km.

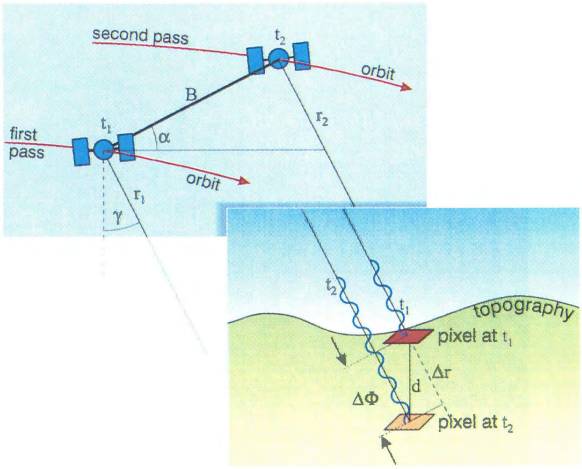

Figure 5. Geometry of InSAR with non-zero baseline. Explanation in text 'Basic principles'.

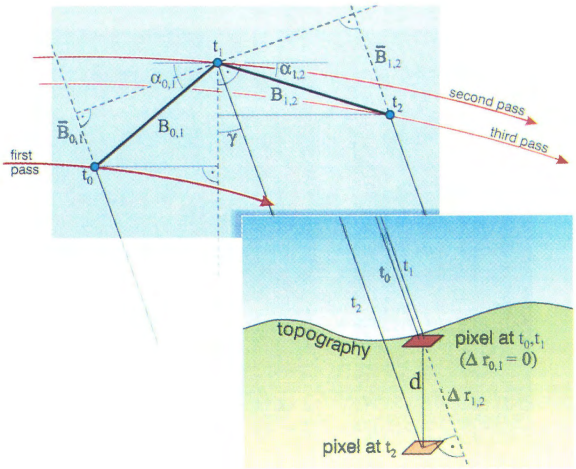

Figure 6. Geometry of differential InSAR.

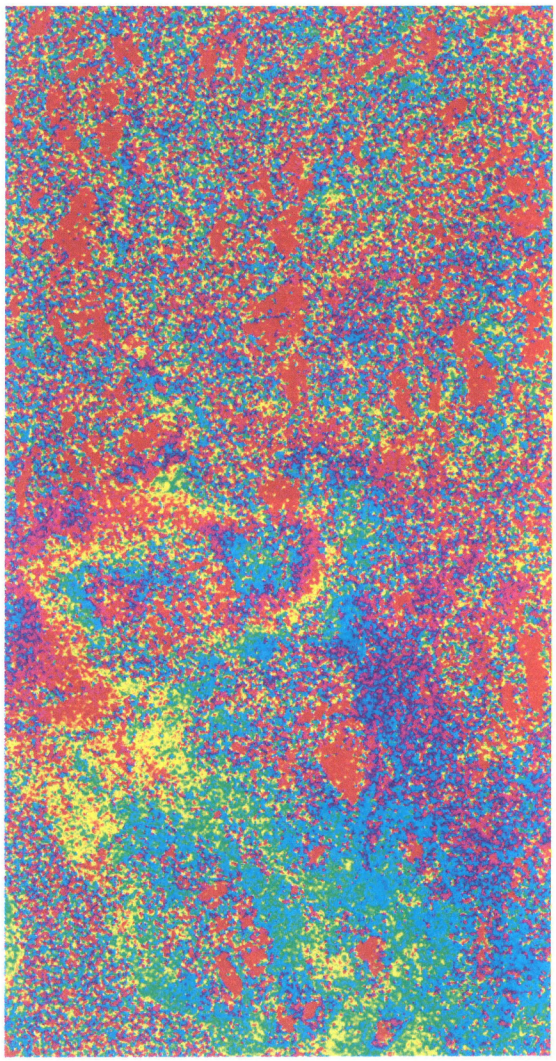

Figure 7. Deformation field of the M = 6.7, 18 June 1994, Arthur's pass earthquake in the Southern Alps of New Zealand, mapped by InSAR. North to the top; scale is 50 m a pixel; image size is 51.2 km in E–W, and 94.6 km in N–S direction.

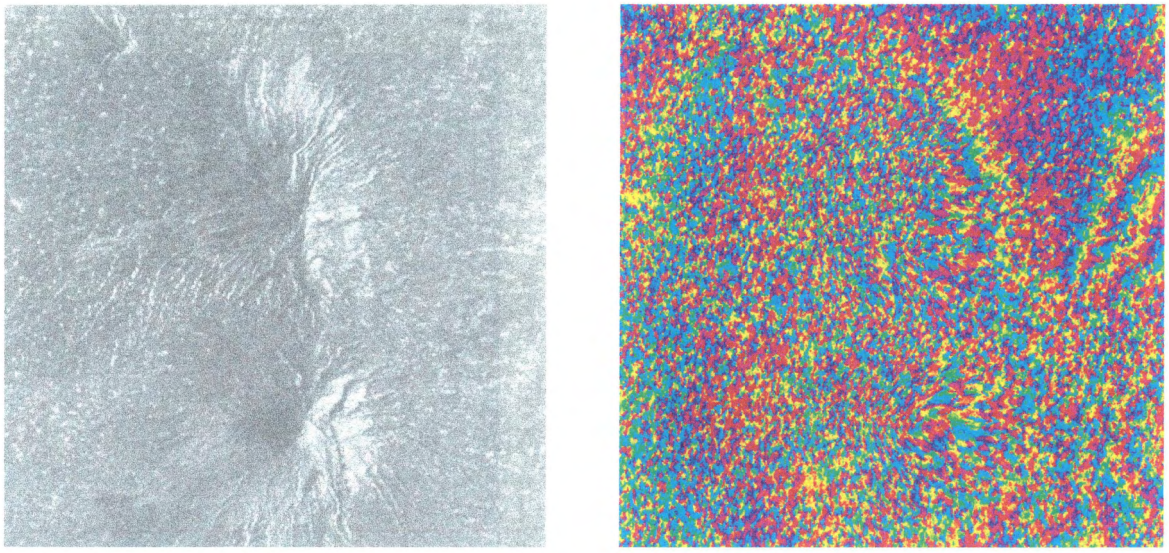

Figure 8. JERS-1 amplitude image (left) and interferogram (right) of the area around Merapi (south/bottom) and Merabu (north/top) volcanoes, near Yogyakarta in central Java, Indonesia. Scale is 40 m a pixel (no other information available to the authors).

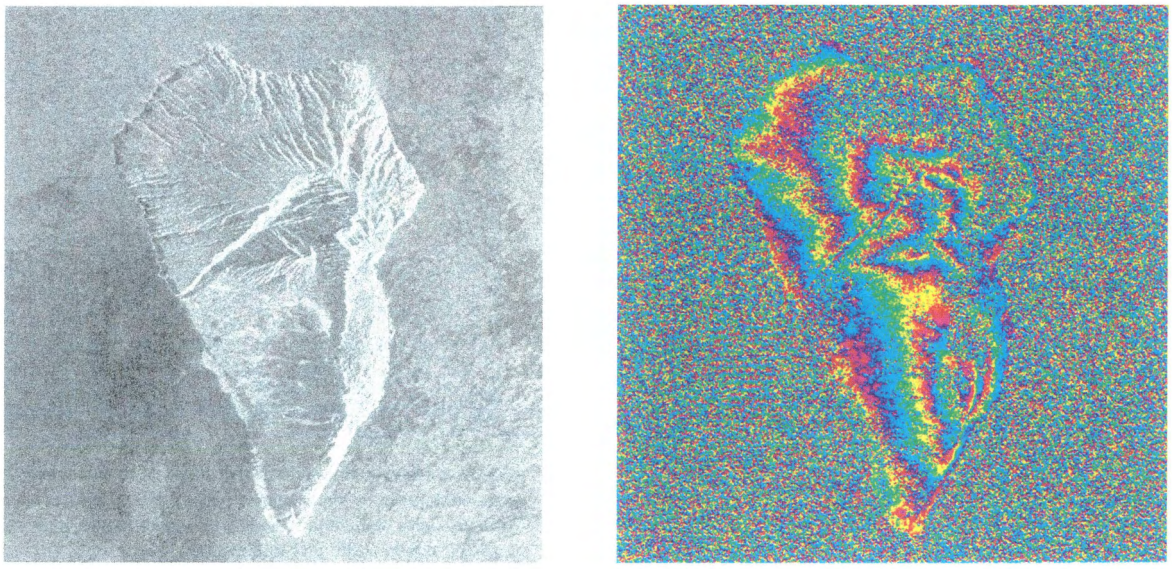

Figure 9. Amplitude image (left) and uncorrected interferogram (right) of La Palma island, Atlantic Ocean. North to the top; image size is ca. 50 × 30 km.

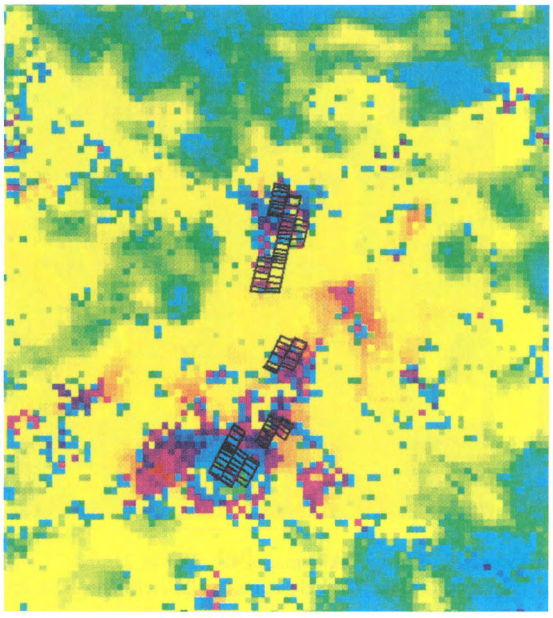

Figure 10. Close-up of interferogram of Gardanne mining site, France. The area covers ca. 8.4 × 9.4 km, the pixel size is 100 m. Superimposed is the mining schedule since 1990 (from Carnec et al. 1996).

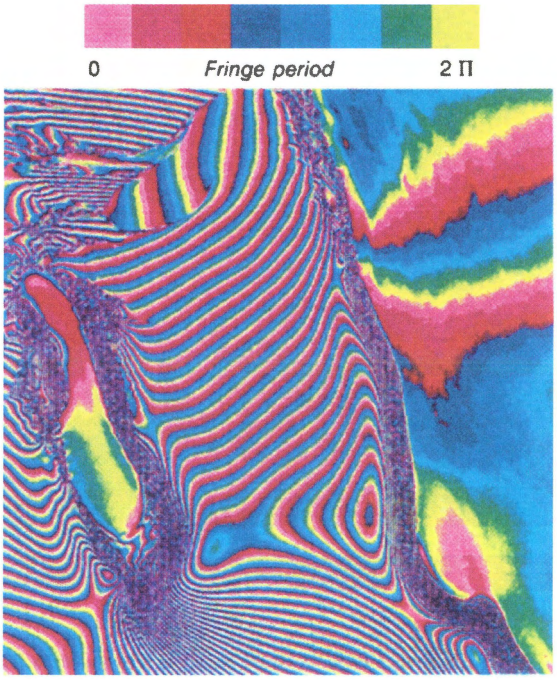

Figure 11. SAR interferogram of the Filchner-Ronne shelf ice in the Antarctic (from Hartl et al. 1994). We see on the right side the western slope of Berkner Island resting on bedrock, and on the left Hemmen Ice Rise grounded on sea-bed shoals and surrounded by the floating Ronne Ice Shelf.

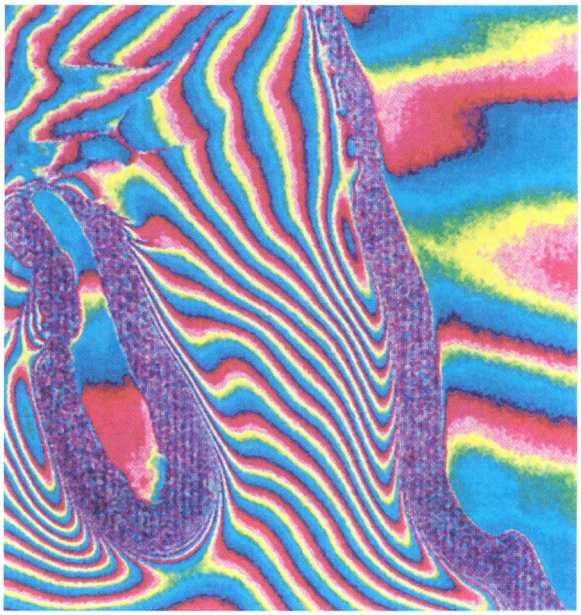

Figure 12. Differential SAR interferogram of the Filchner-Ronne shelf ice showing differences in the tidal signal at the data acquisition times (from Hartl et al. 1994). The rise and fall of the ocean tide and the seaward movement of the ice can be seen in the fringe pattern towards the top of the image.

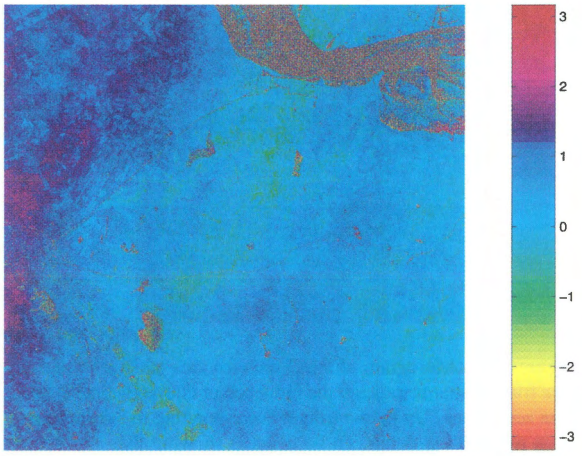

Figure 14. ERS tandem mission interferogram of the Groningen area, the Netherlands, from SAR images acquired at 26 and 27 February 1996, at 10:29 UTC (from Hanssen & Feijt 1996) showing phase changes of 11 mm. The effect of topography in this flat terrain can be almost neglected, changes due to surface deformation within a one-day period are unlikely. Therefore, the observed phase change represents disturbing effects possibly attributable to atmospheric perturbations. North to the top; image size is ca. 50 × 50 km.

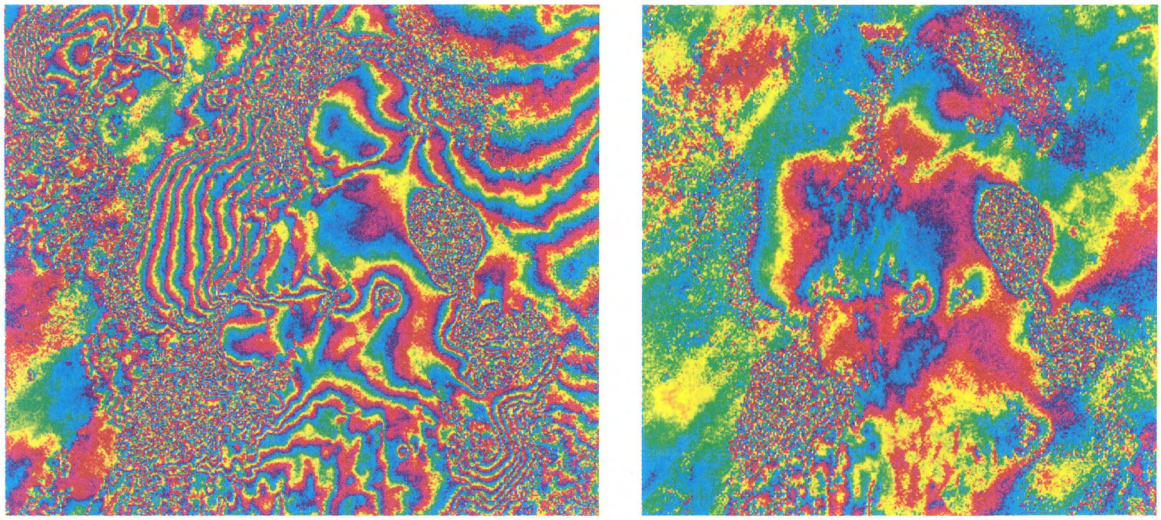

Figure 13. Interferograms of the area around Vatnajökull volcano on Iceland formed by SAR images acquired at 21 and 22 October 1996. Topography (left) and subsurface deformation (right). One fringe corresponds to ca. 72 m elevation change (left) and 3 cm vertical deformation (right), respectively (from Thiel et al. 1997).

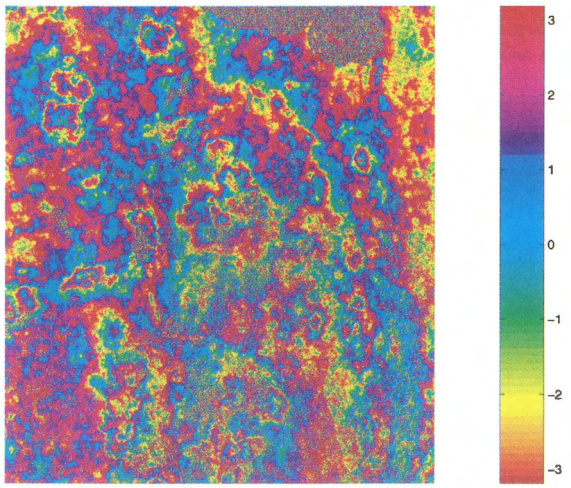

Figure 16. Interferogram of the Groningen area taken over one day. The fringe patterns indicate the influence of convective cells during data acquisition. Up to two fringes corresponding to 5.6 cm line-of-sight propagation delay can be counted showing that atmospheric effects can have a very large influence on the interferogram (from Hanssen & Usai 1997). North to the top; image size is ca. 50 × 50 km.

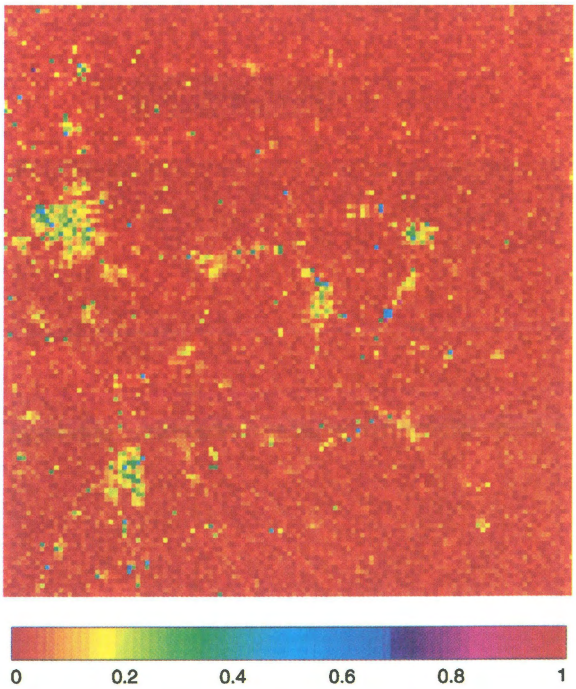

Figure 18. Coherence image for the Groningen area shown in Figure 16, for 3.5 years using 20 × 110 independent samples per pixel. The image pair contains information which may be used to extract phase values (from Hanssen & Usai 1997). North to the top; image size is ca. 50 × 50 km.

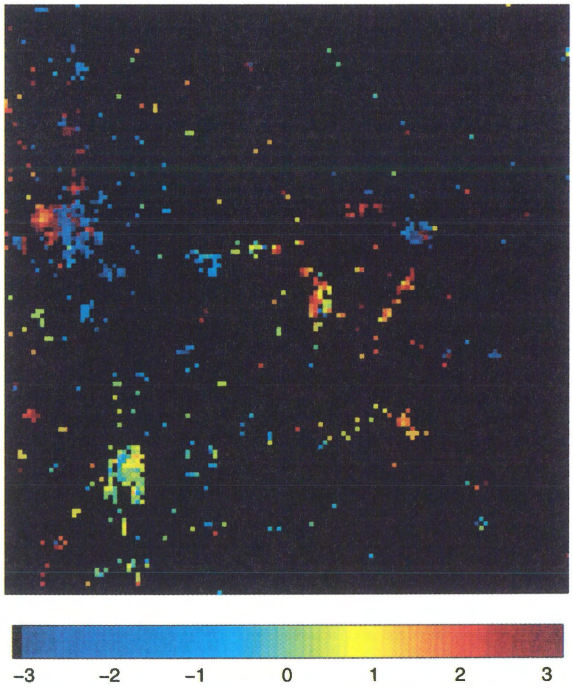

Figure 19. Masked interferogram for the Groningen area shown in Figure 16 (threshold 0.1) for a multilook window of 20 by 110 pixels (from Hanssen & Usai 1997) showing that the extraction of deformation signature is possible by eliminating those pixels with high satellite orbit errors and with disturbance due to atmospheric perturbations. North to the top; image size is ca. 50 × 50 km.